Electronic Supplementary Information (ESI)

ENHANCED BACTERICIDAL ACTIVITY OF BRUCITE THROUGH PARTIAL COPPER SUBSTITUTION

Batiste CLAVIER [1], Téo BAPTISTE [1], Florian MASSUYEAU [2], Alain JOUANNEAUX [1],

Amandine GUIET [1], Fabien BOUCHER [3], Vincent FERNANDEZ [2],

Christine ROQUES [4] and Gwenaël CORBEL [1*]

[1] Institut des Molécules et Matériaux du Mans (IMMM), UMR-6283 CNRS, Le Mans Université, Avenue Olivier Messiaen, 72085 Le Mans Cedex 9, France

[2] Institut des Matériaux Jean Rouxel (IMN), UMR-6502 CNRS, Université de Nantes, 2 rue de la Houssinière, BP32229, 44322 Nantes cedex 3, France

[3] Institut Universitaire de Technologie du Mans, Le Mans Université, Avenue Olivier Messiaen, 72085 Le Mans Cedex 9, France

[4] Laboratoire de Génie Chimique, UMR-5503 CNRS, Faculté de Pharmacie, Université Paul Sabatier - Toulouse III, 35, chemin des maraîchers, 31 062 Toulouse Cedex 4, France

[*] To whom correspondence should be addressed
Institut des Molécules et Matériaux du Mans (IMMM)
UMR-6283 CNRS, Le Mans Université
Avenue Olivier Messiaen, 72085 Le Mans Cedex 9, France
Tel : +33 (0)2 43 83 26 48 FAX : +33 (0)2 43 83 35 06
E-mail : gwenael.corbel@univ-lemans.fr
ORCID : 0000-0003-2605-7702

1. Experimental

1.1 Starting materials.

$Mg(NO_3)_2.6H_2O$ (Alfa Aesar, 98%), HNO_3 (VWR Chemicals, 68%), NaOH (Sigma-Aldrich, 98% pellets) and Na_2CO_3 (Acros Organics, 99.8%) were used as received. Commercial CuO (Alfa Aesar, 97%) contains a small amount of cuprous oxide Cu_2O. Prior to use, powder of CuO, spread over the bottom of an alumina boat, was therefore annealed at 600°C for 12 h in a pure dioxygen gas flow (1 atm) to fully oxidize cuprous ions.

1.2 Synthesis.

Mixed hydroxides "$Mg_{1-x}Cu_x(OH)_2$" were prepared at room temperature by coprecipitation synthetic route. In a Teflon beaker, a stoichiometric amount of CuO and $Mg(NO_3)_2.6H_2O$ were first dissolved at room temperature in 20 mL of concentrated HNO_3. After homogenization for 30 min under stirring, the blue solution was heated up to 140°C on a hot plate to slowly evaporate the excess of acid and to obtain a blue solid corresponding to intimate mixture of copper and magnesium nitrates. A 0,5 M mixed metal nitrate solution was then prepared by dissolving the ground blue solid in 50 mL of deionized water. This as-prepared solution was subsequently added dropwise to 150 mL of a freshly prepared mixture of 0,6 M NaOH and 0,1 M Na_2CO_3 solutions. Upon addition, pH slightly increases from 12.5 to 13.8 depending on the copper content x (Fig. S1).

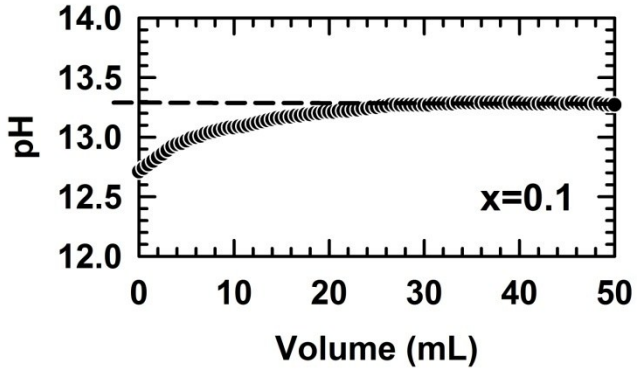

Fig. S1 : Evolution of the pH of freshly prepared mixture of 0,6M NaOH and 0,1M Na_2CO_3 solutions when the volume of the 0,5M mixed metal nitrates solution was added dropwise in order to form particles of $Mg_{0.9}Cu_{0.1}(OH)_{2-2y}(CO_3)_y.zH_2O$ (x=0.1).

Precipitation occurred at room temperature instantaneously upon addition of the first drop of the mixed nitrate solution, thus changing the colorless solution into a solution with blue particles in suspension. After complete delivery of the mixed nitrate solution, the suspension

was stirred for 30 min and then aged for 3 h without stirring. A full decantation by gravity of particles took place during this ageing period. The absorption spectrum collected on the colorless supernatant (Fig. S2) did not exhibit a broad peak in the wavelength range 500-1000 nm characteristic of d-d electronic transition of square planar $[Cu(OH)_4]^{2-}$ anion [1] or solvated divalent copper in octahedral coordination [2], thus confirming its complete precipitation.

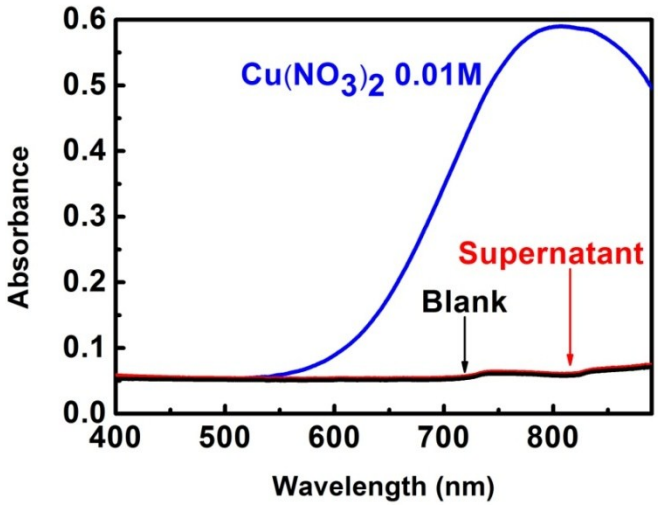

Fig. S2 : The absorption spectrum collected on the colorless supernatant after a full decantation by gravity of particles of $Mg_{0.9}Cu_{0.1}(OH)_{2-2y}(CO_3)_y.zH_2O$ (x=0.1) taking place during this ageing period of 3h.

To remove sodium and carbonate ions, the resulting precipitate was washed with deionized water and centrifuged several times at 4000 rpm for 2 min by using an Eppendorf 5804R centrifuge. After the last washing with water, the liquid was drawn through a Büchner funnel by vacuum suction to recover the solid on a filter paper. The resulting powder was dried in air at 60°C for 12 h and grinded for 5 min with hand mortar and pestle.

1.3 X-Ray Powder Diffraction (XRPD).

The phase purity of as-prepared and dehydrated powders was checked by recording X-ray powder diffraction (XRPD) patterns at room temperature on a PANalytical θ/θ Bragg-Brentano Empyrean diffractometer ($CuK\alpha_{1+2}$ radiations) equipped with the PIXcel^{1D} detector. The raw and dehydrated powders were dusted through a 160 µm sieve on a glass holder. XRPD patterns were collected at room temperature in the [5°-135°] scattering angle range, with a 0.0131° step size, for a total acquisition time of 331 min.

Thermal decomposition in air of as-prepared powders was studied by temperature-controlled X-ray powder diffraction. Temperature-controlled XRPD patterns were recorded on the same diffractometer at 25°C intervals between 25 and 400°C (heating rate of 10°C/min,

temperature stabilisation for 20 min, cooling rate of 60°C/min, air flow of 40 mL/min) by using an XRK 900 Anton Paar reactor chamber. The sample was deposited on the sieve (pore size ∅ 0.2mm) of the open sample holder cup, both made of glass ceramic Macor ® , thus allowing gas to flow through the sample. XRPD pattern was collected at each temperature in the [10°-100°] scattering angle range, with a 0.0131° step size, for a total acquisition time of 180 min.

The integral-breadth apparent size ε_β of nanometer-sized particles after dehydration at 200°C (hereafter referred to as dehydrated powders) was determined from diffraction data by the Integral Breadth method [3-6]. The instrumental resolution function of the Empyrean diffractometer was first determined on the Reference Material $Na_2Ca_3Al_2F_{14}$ (NAC [7]) whose XRPD pattern was recorded with the same data collection conditions as those used for dehydrated powders. The pattern was then refined by the Le Bail method [8] with the Fullprof program [9] using a modified Thompson-Cox-Hastings pseudo-Voigt profile function [10] (referred to as TCH-Z function) in which the size-broadening and microstrain-broadening effects both contribute to the Lorentzian and Gaussian components of the line widths. In a second step, the diffractogram of dehydrated powders were then modelled by the Le Bail method [8] using this instrumental resolution TCH-Z function and selecting the "Platelet vector size" model of the Fullprof program [9]. The two parameters of the Lorentzian component of this TCH-Z function were only refined to calculate the average integral-breadth apparent size $<S_\beta>$ for each (hkl) reflection.

1.4 Infrared (IR) spectroscopy.

IR transmission spectra were collected on as-prepared polycrystalline samples in air at room temperature with an Alpha Bruker Fourier transform infrared (FT-IR) spectrometer equipped with the "Platinum" QuickSnap™ ATR sampling module. Each spectrum was obtained after 25 scans in the 4000-400 cm^{-1} range with a spectral resolution of 4 cm^{-1}. A reference IR spectrum was collected in the same conditions without any sample and subtracted to spectra collected on specimens in order to remove the contribution of atmospheric water vapour and carbon dioxide gas.

1.5 Thermal analyses.

The thermal decomposition of as-prepared powders was studied by thermogravimetric (TG) and Mass Spectrometric (MS) evolved gas analyses. Desorption of water molecules adsorbed on the particle surface was carried out in static air at 60°C prior to any analysis. Thermal analyses were then performed from room temperature to 800°C on a Jupiter NETZSCH

STA449 F3 thermogravimetric analyser by heating at 2°C/min about 50 mg of degassed sample in open alumina crucible under a controlled argon flow of 60 mL/min. Three cycles of vacuum purging were performed before starting the experiment in order to remove any trace of atmospheric gases (N_2, O_2, CO_2 and of water vapour) present in the thermobalance. The gases evolved in the thermal analyses were monitored with a Aeolos Quadrupole Mass Spectrometer 403C coupled to the thermal balance via a stainless steel capillary heated to 250°C. The mass gates used were m/z 17 (OH), 18 (H_2O), 28 (CO), 30 (NO), 44 (CO_2) and 46 (NO_2).

1.6 Optical absorption spectroscopy.

UV-Visible-Near-IR optical absorption spectra were measured on solutions and raw powders by using two different apparatus. For solutions, spectra in the range 400-1400 nm were recorded on a Shimadzu UV-2600 spectrophotometer. For powders, the previous spectrophotometer was equipped with an integrating sphere ISR-2600plus. The spectral resolution is 1 nm in the 400-1400 nm. At Near-IR wavelengths higher than 1350 nm, spectra were recorded on a Lambda 1050 Perkin Elmer spectrophotometer equipped with a tungsten lamp, an InGaAs detector and a 150 mm integrating sphere. A spectral bandwidth of 1 nm and an acquisition time of 0.2 s were used for these last measurements.

1.7 Transmission Electron Microscopy (TEM).

The TEM study was performed on a JEOL JEM 2100 HR electron microscope operating at 200 kV and equipped with a side entry ±35° double-tilt specimen holder. The sample for transmission electron microscopy investigation was prepared by ultrasonically dispersing the raw powder in absolute ethanol, depositing a drop of the resulting suspension onto a holey carbon-coated copper grid (or nickel grid for EDX analyses) and finally drying the grid in air. Chemical analysis was done on a large number of individual particles with an Energy-Dispersive X-ray (EDX) spectrometer JEOL JED-2300 T attached to the microscope.

1.8 Nitrogen sorption measurements.

N_2 adsorption measurements were performed at 77 K on a Micromeritics TriStar II 3020 Instrument (Micromeretics, Norcross, GA). Prior to any surface area measurement, water vapour and gases adsorbed onto the grain surface were desorbed under primary vacuum by using the Micromeritics VacPrep 061 degasser. Approximately 400 mg of powder was employed in each measurement. All samples exhibit a type II adsorption isotherm typical of nonporous solids. The specific surface area was calculated using the Brunauer−Emmet−Teller (BET) model [11].

1.9 X-ray Photoelectron Spectroscopy (XPS).

The X-ray photoelectron spectra were recorded on a Kratos Nova apparatus using a monochromated Al Kα source 1486.6 eV. The instrument base pressure was 5×10^{-10} Torr. The sample area analyzed was about 700 µm × 300 µm. A Pass Energy (PE) of 160 eV or 80 eV, corresponding to an all over Silver Fermi edge resolution of 1.86 ± 0.06 eV or 0.95 ± 0.03 eV with an energy step of 0.5 eV, was used to acquire wide range survey spectra. High resolution Cu $2p_{3/2}$ core-level spectrum in a narrow binding energy range were performed at a PE of 40 eV, corresponding to an all over Silver Fermi edge resolution of 0.56 ± 0.02eV eV with an energy step of 0.5 eV. This acquisition mode allows to have a good resolution in a short measuring time (16 min) while minimizing the exposure of samples to X-Rays. This mode was also used to follow the *in-situ* reduction of samples as a function of the exposure time. All data were acquired using the Kratos charge neutralizer system to establish a steady state surface potential. Raw powders were maintained on conductive adhesive double side tape. XPS data including peak fitting, line shape synthesis, envelope background modeling with a Tougaard function [12] and subtraction/quantification of components was processed using *CasaXPS* program [13] (suite versions 2.3.17 to 2.3.23).

1.10 Microwave Plasma - Atomic Emission Spectroscopy (MP-AES).

Atomic Emission spectroscopy has been used for measuring the amount (down to 0.05 ppm) of magnesium and copper elements possibly released from mixed hydroxides "$Mg_{1-x}Cu_x(OH)_2$" when immersed in deionized water. Particles are immersed in deionized water at a final concentration of 1 mg/mL without agitation for 3 h or 24 h. Concentration in magnesium and copper ions released by hydroxides particles was determined by using a 4100 Micro Plasma - Atomic Emission Spectrometer (MP-AES) from Agilent Technologies. The apparatus is equipped with a OneNeb nebulizer and a double-pass cyclonic spray chamber. The analytical cycle consisted of 15 s of sample uptake (pump speed 40 rpm) then 15 s of stabilization before performing three replicates. Calibration solutions were prepared by dilution of the ICP multi-element standard VIII solution (100 mg/L, Merck) in the range 0.05-10 mg/L. 5 mL of supernatant solution was manually introduced by using a capillary. When concentration in cations was above the calibration range, a dilution was then carried out. Integration time was set to 3s both for magnesium and copper ions. Background was automatically subtracted from the signals by activating the blank subtraction mode of the MP Expert software from Agilent Technologies. The peak intensity were also determined by this software. Calibrations functions for the MP-AES measurements were linear up to 10 mg/mL

for copper ions ($r^2 > 0.999$, 324.754 nm) and 5 mg/mL for magnesium ions ($r^2 > 0.995$, 285.213 nm).

1.11 pH measurement of particle suspension.

Particles are immersed in deionized water at a final concentration of 1 mg/mL without agitation. At regular intervals between 15 min and 24 h, pH of the aged solution was then measured at room temperature with a SCHOTT GERÄTE CG818 pH-meter.

1.12 Bactericidal activity experiments.

The evaluation of the bactericidal activity of the hydroxide particles was carried out at 20°C against two strains obtained from the Institute Pasteur Collection (Paris, France) : *Staphylococcus aureus* CIP 4.83 and *Escherichia coli* CIP 53126. The strains were stored at -80°C in Eugon broth (AES, Rennes, France) with 20% (v/v) glycerol (Fluka, Butch, Switzerland). Before each experiment, preserved bacteria were grown at 36°C under aerobic conditions on trypticase soy agar medium during 24h (Biomérieux, Craponne, France). The second and third subcultures were used to extemporaneously prepare suspensions with a concentration in bacteria of about 2×10^8 Colony Forming Units per mL (CFU/mL calculated from the Optical Density measured at 640 nm). The as-prepared hydroxide particles were dispersed at 20°C in sterile distilled water to obtain a suspension with an initial concentration of 1mg/mL. For each strain, 10 mL of the particles suspension is inoculated into 100µL of bacterial suspension, thus leading to a final concentration in bacteria of $\approx2\times10^6$ CFU/mL. A bacterial suspension without particles was used as a positive control. The suspension of particles in contact with bacteria was maintained at 20°C under constant stirring on a rotary platform working at 250 shakes per min. At specified times (15 min, 30 min, 1 h and 3 h), 1 mL of the suspension and of the serial ten-fold dilutions were incorporated into trypticase soy agar medium poured in flat-bottomed Petri plates and were incubated at 36°C for 24 or 48 h. The viable cell number was determined by counting the number N of bacterial colonies grown (CFU = Colony Forming Units), multiplied by the dilution factor and expressed as CFU/ml. Results are expressed in CFU counts N_t at a contact time t (N_0 at t = 0), in R $\log_{10}$ reduction ($R = \log_{10}(N_0/N_t)$) and in percent reduction in cell viability $[(N_0-N_t)\times100]/N_0$. The experiments were repeated two times for each strain tested. For each contact time tested, control numerations of CFU/mL were also performed in sterile distilled water and without particles. The cell viability was preserved for both bacteria in these conditions because the CFU counts N_t at t = 15, 30, 60 and 180 min remain constant regarding the counts N_0 at t=0 min. The reduction in cell viability in such assay conditions only occurs for longer contact time.

2. Origin of the lattice expansion when dehydrating samples.

When compared with the XRPD patterns of the as-prepared hydroxides also collected at room temperature and displayed in Fig. 1a of the article, one can note that the position of the (001) peak for a given composition has slightly shifted towards the low scattering 2θ angles after dehydration (Fig. 1b). It means that the interlayer galleries weakly expand in height along the c axis when removing water molecules in $Mg_{1-x}Cu_x(OH)_{2-2y}(CO_3)_y.zH_2O$ hydroxides. Jobbagy *et al.* [14] have probed by XRPD the effect of Relative Humidity (RH) at room temperature on the crystal structure of several Layered Double Hydroxides (LDH) as for instance $Mg_6Al_2(OH)_6(CO_3).4H_2O$. Since an equilibrium between the water partial pressure and the water content of LDH occurs, a continuous decrease in RH naturally induces a soft dehydration of LDH. This dehydration here induces a shrinkage along the stacking direction of Brucite-type layers giving rise to a displacement of (00*l*) diffraction peaks towards the low scattering 2θ angles. In LDH, the dehydration is topotactic in nature since only the gallery height decreases. If the dehydration process in $Mg_{1-x}Cu_x(OH)_{2-2y}(CO_3)_y.zH_2O$ hydroxides is also fully topotactic, the associated lattice expansion can be, in this respect, counter-intuitive or unexpected. Is it really the case?

By paying attention on the presence of pillars in the structure of $Mg_{1-x}Cu_x(OH)_{2-2y}(CO_3)_y.zH_2O$ hydroxides, an explanation of the lattice expansion along the c axis generated by the dehydration can be proposed. No water molecules are present in the galleries of the Aurichalcite $Zn_3Cu_2(OH)_6(CO_3)_2$ [15], certainly due to the steric hindrance between pillars and water molecules. In this structure, one $[M3O_4]$ tetrahedron and one triangular carbonate group share a vertex to form a pillar. This connection mode is comparable to a knee joint that can fold and unfold thanks to a rotation of the carbonate group. In the $Mg_{1-x}Cu_x(OH)_{2-2y}(CO_3)_y.zH_2O$ hydroxides, both contents in water molecules (z) and carbonate groups (y) are very small (Table 1 in the article). Certain galleries of these mixed hydroxides are certainly free of water molecules while others are partially filled. By taking into account the steric hindrance between pillars and water molecules, one can consider that :

i) the galleries of the mixed hydroxides, free of water molecules, are those having pillars and *vice-versa*.

ii) because of small amount of carbonate groups (y), the number of pillars per gallery in the $Mg_{1-x}Cu_x(OH)_{2-2y}(CO_3)_y.zH_2O$ structure is lower than that found in one pillared gallery of the Aurichalcite $Zn_3Cu_2(OH)_6(CO_3)_2$ structure.

iii) the pillars are randomly and homogeneously distributed within galleries of the $Mg_{1-x}Cu_x(OH)_{2-2y}(CO_3)_y.zH_2O$ structure.

Note that, the height of galleries in dehydrated (idealized) $Mg(OH)_2$ (2.689 Å [16]) is more than two times smaller than the height of galleries (5.688 Å) in Pyroaurite $Mg_6Fe_2(OH)_{16}(CO_3).4H_2O$ [17, 18]. To accommodate the water molecules in a gallery of the idealized Brucite $Mg(OH)_2$ structure, the host gallery must locally expand in height. Such insertion is possible in the $Mg_{1-x}Cu_x(OH)_{2-2y}(CO_3)_y.zH_2O$ structure because the adjacent gallery can locally contract in height thanks to a folding of the "[MgO_4] tetrahedron-carbonate" joint (Fig. S3b). In that way, the Brucite-type structure can globally be preserved for the $Mg_{1-x}Cu_x(OH)_{2-2y}(CO_3)_y.zH_2O$ samples (Fig. S3b) but the stacking of layers is now disordered as stated in the section 2.1 of the article. The dehydration would induce, at reverse, the unfolding of this joint (Fig. S3c) because the galleries in which water molecules were previously hosted recover their natural height. The height of these water-free galleries should be close to that of galleries in dehydrated $Mg(OH)_2$ ≈ 2.7 Å. In Aurichalcite $Zn_3Cu_2(OH)_6(CO_3)_2$ [15], the average height of pillars is ≈ 5.1 Å which is almost two times the height of galleries in dehydrated $Mg(OH)_2$ (2.689 Å [16]). By dehydrating the $Mg_{1-x}Cu_x(OH)_{2-2y}(CO_3)_y.zH_2O$ hydroxides, an expansion in length of the c axis occurs because the unfolding of the "[MgO_4] tetrahedron-carbonate" joint induces an expansion in height of pillared galleries larger in magnitude than the reduction in height of galleries releasing the water molecules they hosted (Fig. S3c). The value of the c parameter is then dependent on the number of pillared galleries (linked with the carbonate content y) of the dehydrated $Mg_{1-x}Cu_x(OH)_{2-2y}(CO_3)_y$ sample. This value determined from the diffraction data (Fig. 7b in the article) is therefore a mean <c> value. If c_B and c_{PB} are the cell parameters of the dehydrated/idealized $Mg(OH)_2$ Brucite and of a "fully Pillared Brucite" (which does not exist in nature) respectively, the mean value <c> can be defined as follows : $<c> = 1/(n+m)\times[n\times c_B+m\times c_{PB}]$ where n and m are the numbers of dehydrated and pillared galleries, respectively (Fig. S3c). Obviously, this formula does not take into account the possible impact of copper substitution on the <c> parameter but it highlights how complex is the structure of dehydrated $Mg_{1-x}Cu_x(OH)_{2-2y}(CO_3)_y$ samples. This proposed dehydration mechanism makes sense if we reconsidered the dehydration process of LDH. In carbonate containing LDH (as for instance in $Mg_6Al_2(OH)_6(CO_3).4H_2O$ [19]), the dehydration induces the contraction in length of the c parameter rather than its expansion because triangular CO_3^{2-} anions are free with an orientation parallel to Brucite-type layers (see the crystal structure of Pyroaurite $Mg_6Fe_2(OH)_{16}(CO_3).4H_2O$ [17, 18] shown in Fig. 2 of the article).

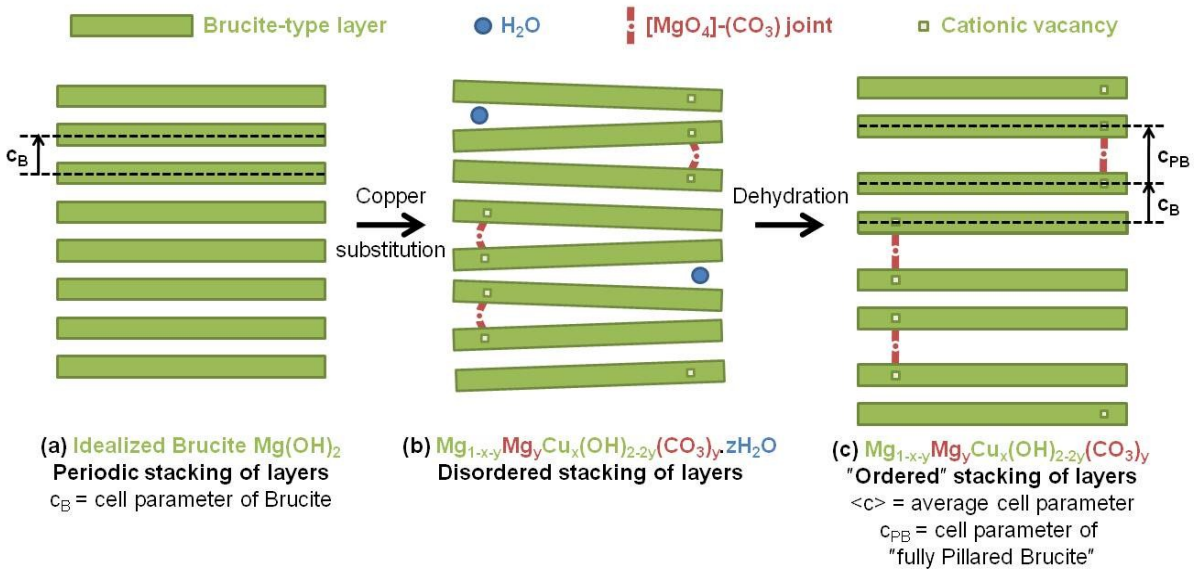

Fig. S3 : Dehydration mechanism in $Mg_{1-x}Cu_x(OH)_{2-2y}(CO_3)_y.zH_2O$ hydroxides.

3. Chemical state of surface particles probed by X-ray Photoelectron Spectroscopy (XPS).

Nano-structuring is known to promote the formation of surface defects (incomplete coordination sphere of cations at the grain surface) which could also lead locally to a slight reduction of cupric ion to cuprous one. A thorough examination of chemical state surface was performed on all $Mg_{1-x}Cu_x(OH)_{2-2y}(CO_3)_y.zH_2O$ samples by X-ray Photoelectron Spectroscopy (XPS) in order to determine the oxidation state(s) of copper ions. In the secondary vacuum condition, a dehydration of the $Mg_{1-x}Cu_x(OH)_{2-2y}(CO_3)_y.zH_2O$ samples certainly occurs. It is not detrimental to the present study because the dehydration preserves the Brucite-type structure, as shown in Fig. 4 of the article. The XPS analyses are thereby probably performed on dehydrated $Mg_{1-x}Cu_x(OH)_{2-2y}(CO_3)_y$ powders.

The Cu $2p_{3/2}$ core-level spectra of as-prepared hydroxide $Mg_{1-x}Cu_x(OH)_{2-2y}(CO_3)_y.zH_2O$ samples, collected during the first 16min of X-ray exposure, are displayed in Fig. S4. For both samples, the spectra show a broad peak at ≈ 940eV and a second peak of high intensity at ≈ 932eV with a shoulder at lower binding energy around ≈930eV. The peaks at ≈932eV and ≈ 940eV correspond to the $Cu2p_{3/2}$ spin-orbital component and the associated shake-up satellite of Cu^{2+} species, respectively. These two peaks have electron binding energies similar than those reported by Biesinger *et al.* for Cu^{2+} species in $Cu(OH)_2$ [20]. The presence of a shoulder at electron binding energy lower than that of Cu^{2+} species means that a fraction of copper ions in the samples have an oxidation state lower than two (*i.e.* Cu^+ ou Cu^0). As mentioned above,

the presence of Cu^{+} species can be suspected in the $Mg_{1-x}Cu_x(OH)_{2-2y}(CO_3)_y.zH_2O$ samples because of the nanometer size of particles. A partial reduction could also occur in the secondary vacuum condition used within the XPS apparatus. To determine if these cuprous ions are intrinsically present at the surface particles or if they come from an *in-situ* reduction of samples, the copper-rich x = 0.15 and 0.2 samples were continuously exposed to X-rays while acquisition of the Cu $2p_{3/2}$ core-level spectrum was performed periodically. The experiment was performed on each sample for a total time of 800 min with Cu $2p_{3/2}$ core-level spectra acquisition in a narrow binding energy range every 16 min (a total of 50 spectra). Peak fitting was then carried out in order to calculate the relative peak area attributed to cuprous and cupric species. The time dependence of the relative peak area are shown in Fig. S5. When exposed to X-ray radiations in the secondary vacuum condition, the Cu^{2+}/Cu^{+} ratio in both samples rapidly decreases in the first 2 hours. Above this time, the reduction slows down and almost reaches a plateau. After 800 min of irradiation, the relative peak area ascribed to cupric species is 32 % and 26 % in the x = 0.15 and 0.2 samples, respectively (Fig. S5). The reduction of cupric ions is therefore significant but incomplete. A darkening of the powders is then noted at the end of the experiment which is consistent with a segregation of Cu_2O.

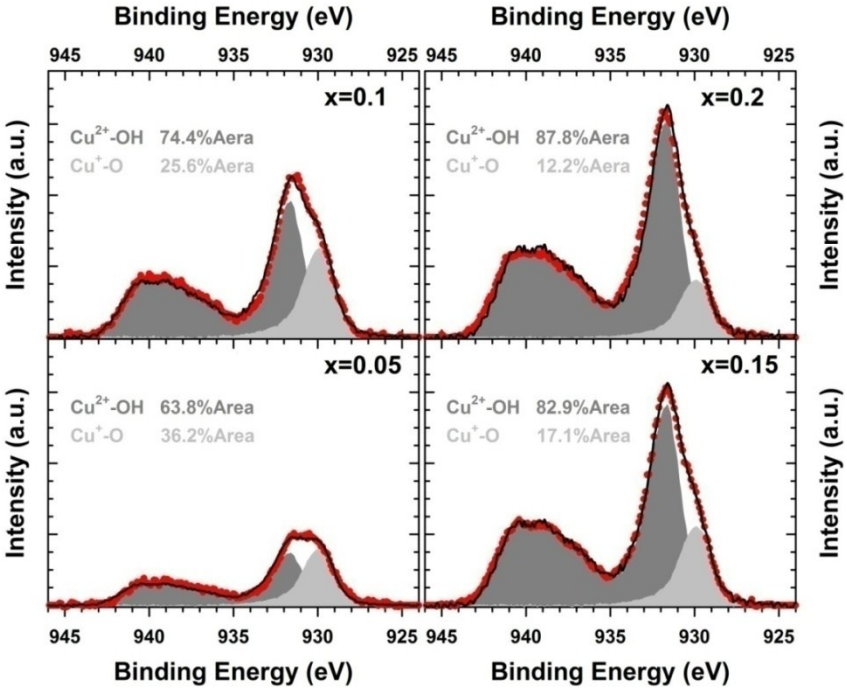

Fig. S4 : Cu $2p_{3/2}$ core level spectra collected during the first 16min of X-ray exposure on as-prepared $Mg_{1-x}Cu_x(OH)_{2-2y}(CO_3)_y.zH_2O$ raw powder samples for different copper contents x. Relative peak area attributed to the different Cu^{2+} and Cu^{+} species are given.

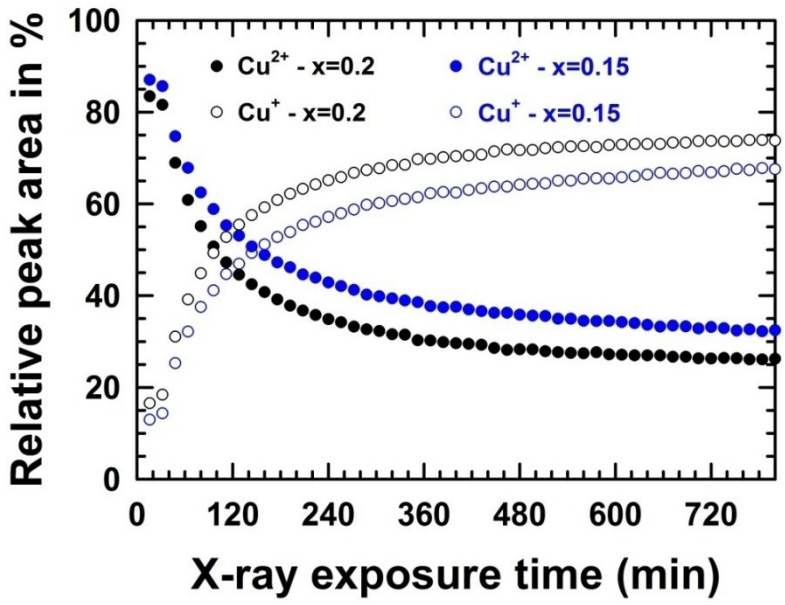

Fig. S5 : Time dependence of the relative peak area attributed to Cu^{2+} and Cu^{+} species in the Cu $2p_{3/2}$ core level spectra collected on $Mg_{0.85}Cu_{0.15}(OH)_{2-2y}(CO_3)_y.zH_2O$ (x=0.15) and $Mg_{0.8}Cu_{0.2}(OH)_{2-2y}(CO_3)_y.zH_2O$ (x=0.2) samples.

Copper hydroxide, $Cu(OH)_2$ decomposes into copper oxide CuO at 145-160 °C and ambient air pressure [21]. Skinner *et al.* [22] have reported that during XPS analysis of $Cu(OH)_2$ specimen, a partial decomposition into cupric oxide CuO occurs in the first 7 minutes of X-ray exposure in the secondary vacuum condition. This behaviour is not surprising because the thermal decomposition of a sample frequently takes place at temperature lower in vacuum conditions than it was at ambient air pressure (the temperature is around 40 °C within our XPS apparatus). This decomposition of $Cu(OH)_2$ is then followed by a partial photo-reduction of CuO into cuprous oxide Cu_2O when the X-ray exposure is prolonged. In this case, the Cu $2p_{3/2}$ core-level spectrum showed the coexistence of three $Cu2p_{3/2}$ spin-orbital components from the hydroxide and both oxides [22]. In the Cu $2p_{3/2}$ core-level spectra of as-prepared hydroxide $Mg_{1-x}Cu_x(OH)_{2-2y}(CO_3)_y.zH_2O$ samples, no contribution from CuO is seemingly detected. A question can be raised : do our spectrum collection conditions avoid the transient formation of CuO in the $Mg_{1-x}Cu_x(OH)_{2-2y}(CO_3)_y.zH_2O$ samples? A $Cu(OH)_2$ sample was prepared by using the synthesis protocol used for mixed hydroxides. The Cu $2p_{3/2}$ core-level spectrum of the as-prepared $Cu(OH)_2$ sample was then collected in the same conditions as those for mixed hydroxides (*i.e.* 16 min of X-ray exposure in secondary vacuum). The peak fitting of the spectrum is displayed in Fig. S6. A third contribution with an electron binding energy (≈ 931eV) corresponding to Cu^{2+} species in CuO [20] was highlighted for our $Cu(OH)_2$

sample, in addition to the two contributions originating from Cu^{2+} species in $Cu(OH)_2$ and Cu^{+} species in Cu_2O. This result is in good agreement with the study of Skinner *et al.* [22].

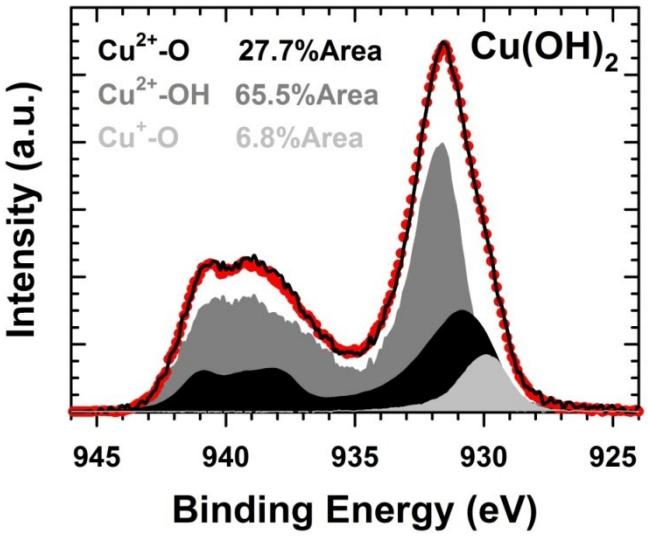

Fig. S6 : Cu $2p_{3/2}$ core level spectrum of the as-prepared $Cu(OH)_2$ raw powder sample. Relative peak area attributed to the different Cu^{2+} and Cu^{+} species are given.

The total and experimental copper content $x_{exp.}$ of each sample was then estimated from the contributions of all copper species detected in the corresponding XPS spectrum collected during the first 16min of X-ray exposure (Fig. S7). This experimental copper content $x_{exp.}$ was found in good agreement with the nominal value for the three first samples of the $Mg_{1-x}Cu_x(OH)_{2-2y}(CO_3)_y$ series. For the most copper-rich composition, a very slight departure from the nominal value is however noticed. From this estimation, the molar fraction of cuprous species is around ≈ 0.02 for all the samples analyzed whatever their nominal copper content x. If this cuprous species would solely originate from the nano-structuring of particles, the amount of cuprous species would rise up with the nominal copper content x of the sample analyzed. It is not the case here. Because no peak ascribed to Cu^{2+} species in CuO was detected in the Cu $2p_{3/2}$ core-level spectrum, $Cu(OH)_2$ and $Mg_{1-x}Cu_x(OH)_{2-2y}(CO_3)_y$ samples behave differently when exposed to X-rays in the secondary vacuum condition. No decomposition of the $Mg_{1-x}Cu_x(OH)_{2-2y}(CO_3)_y$ with a segregation of CuO therefore occurs during the XPS analysis. After XPS analysis, the blue color of copper substituted magnesium hydroxide powders was deeper after X-rays exposition than it was before. Since cuprous oxide is red-brick in color, the powders should turn violet if a segregation of Cu_2O would take place. Thereby, the cuprous species detected after the first 16 min of X-ray exposure would directly result from a partial photo-reduction of a very small amount of cupric species (≈ 2

mol% in Fig. S7) at the grain surface of the mixed hydroxides without any segregation of Cu_2O. Only cupric species are therefore present in as-prepared powders.

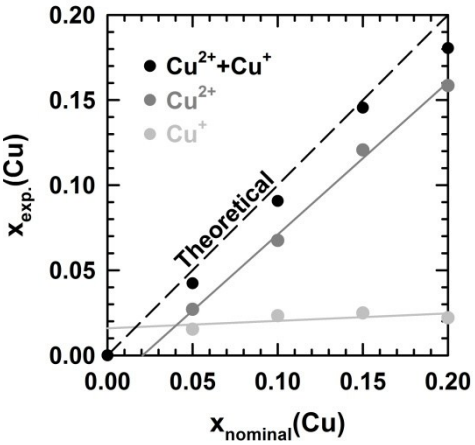

Fig. S7 : Comparison of the total and experimental copper content x_{exp} extracted from the contributions of all copper species detected in the XPS spectra with the nominal value for the as-prepared $Mg_{1-x}Cu_x(OH)_{2-2y}(CO_3)_y.zH_2O$ raw powder samples.

4. References.

1. M. J. Pack, W. Patalinghug and M. T. Weller, *Journal of the Chemical Society-Dalton Transactions*, 1996, **1**, 7-10.
2. D. N. Sathyanarayana, *Electronic Absorption Spectroscopy and Related Techniques*, Universities Press, 2001.
3. J. I. Langford, *J. Appl. Crystallogr.*, 1978, **11**, 10-14.
4. T. H. de Keijser, J. I. Langford, E. J. Mittemeijer and A. B. P. Vogels, *J. Appl. Crystallogr.*, 1982, **15**, 308-314.
5. J. I. Langford, D. Louër, E. J. Sonneveld and J. W. Visser, *Powder Diffraction*, 1986, **1**, 211-221.
6. J. I. Langford, *International Conference "Accuracy in Powder Diffraction II", May 26-29, 1992 at NIST, Gaithersburg, MD, USA*, 1992, 110-126.
7. G. Courbion and G. Ferey, *Journal of Solid State Chemistry*, 1988, **76**, 426-431.
8. A. Le Bail, H. Duroy and J. L. Fourquet, *Materials Research Bulletin*, 1988, **23**, 447-452.
9. J. Rodriguez Carvajal, *Physica B*, 1993, **192**, 55-69.
10. P. Thompson, D. E. Cox and J. B. Hastings, *J. Appl. Crystallogr.*, 1987, **20**, 79-83.
11. S. Brunauer, P. H. Emmett and E. Teller, *Journal of the American Chemical Society*, 1938, **60**, 309-319.
12. M. P. Seah, I. S. Gilmore and S. J. Spencer, *Surface Science*, 2000, **461**, 1-15.
13. N. Fairley, http://www.casaxps.com/, Copyright © 2016 Casa Software Ltd.
14. M. Jobbagy and N. Iyi, *Journal of Physical Chemistry C*, 2010, **114**, 18153-18158.
15. M. M. Harding, B. M. Kariuki, R. Cernik and G. Cressey, *Acta Crystallographica Section B*, 1994, **50**, 673-676.
16. L. Desgranges, G. Calvarin and G. Chevrier, *Acta Crystallographica Section B*, 1996, **52**, 82-86.
17. R. Allmann, *Acta Crystallographica Section B*, 1968, **24**, 972-977.

18. L. Ingram and H. F. W. Taylor, *Mineral. Mag.*, 1967, **36**, 465-479.
19. S. K. Yun and T. J. Pinnavaia, *Chem. Mat.*, 1995, **7**, 348-354.
20. M. C. Biesinger, L. W. M. Lau, A. R. Gerson and R. S. C. Smart, *Applied Surface Science*, 2010, **257**, 887-898.
21. J. R. Gunter and H. R. Oswald, *Journal of Applied Crystallography*, 1970, **3**, 21-26.
22. W. M. Skinner, C. A. Prestidge and R. S. C. Smart, *Surf. Interface Anal.*, 1996, **24**, 620-626.